Article | Received 28 May 2025; Revised 27 October 2025; Accepted 7 November 2025; Published 24 November 2025
https://doi.org/10.55092/esp20250005

Performance and complexity trade-offs of MUSIC-based 2D localization strategies with elevated URAs

Thiago Augusto Bruza Alves*, Bruno Felipe Costa and Taufik Abrão

Department of electrical engineering, State University of Londrina, Londrina, Brazil

* Correspondence author; E-mail: thiago.bruzaalves@uel.br.

Highlights:

- Comparative study of five low-complexity MUSIC-based 2D localization strategies.
- Analysis of accuracy (RMSE) versus SNR and versus number of snapshots (L).
- PEACH-MUSIC exhibits the shortest mean execution time among the evaluated methods, demonstrating reduced computational complexity compared to other search-based approaches.
- We identified techniques that achieve near-CRB accuracy with reduced computational burden.

Abstract: Accurate localization methods are a fundamental component of integrated sensing and communication (ISAC) systems, where sensing and positioning functions must coexist with communication tasks under tight resource constraints. In this work, we provide a comparative study of several classical and low-complexity strategies for two-dimensional (2D) localization with elevated uniform rectangular array (URA) by exploiting known communication pilot signals, a foundational scenario in ISAC. The evaluated techniques include standard MUSIC NF, 2D MUSIC, Adaptive Grid Search (Zoom-in), root-MUSIC, 2D ESPRIT, PEACH-MUSIC, DFT-NF beamforming, OMP NF and a bicubic interpolation refinement of the MUSIC pseudospectrum. The considered system consists of a single ground-level user and an elevated URA under free-space line of sight (LOS) propagation. The methods are assessed in terms of localization accuracy root mean square error (RMSE) versus signal-to-noise ratio (SNR) dB, localization accuracy (RMSE) versus number of snapshots and computational complexity (Mean execution time), highlighting the trade-offs between RMSE × SNR and execution time. Results demonstrate that while classical MUSIC achieves high precision at the expense of prohibitive search complexity, tested search-free methods such as Root-multiple signal classification (MUSIC) and 2D-ESPRIT exhibit performance degradation due to near-field (NF) mismatch but provide competitive accuracy with substantially reduced runtime in compatible conditions. Bicubic interpolation improves the coarse MUSIC grid estimates with negligible overhead, and PEACH-MUSIC demonstrates the lowest runtime among the evaluated algorithms in favorable SNR conditions, while its performance degrades at lower SNR due to reduced spatial diversity. These findings offer a quantitative comparison to guide the selection of localization algorithms where performance and complexity must be carefully balanced, a common requirement in ISAC-oriented architectures.

Keywords: 2D localization; elevated URA; MUSIC; ESPRIT; bicubic interpolation; PEACH-MUSIC; DFT-NF; OMP NF; computational complexity

1. Introduction

Two-dimensional (2D) localization of signal sources using antenna arrays is a cornerstone problem in radar, sonar, and wireless communications, and it also represents a core function within the emerging ISAC paradigm. Accurate and efficient position estimation in the plane is increasingly critical for emerging applications such as fifth and sixth-generation (5G/6G) networks, autonomous systems, smart cities, and extended reality (XR) [1]. For scenarios requiring the estimation of both azimuth and elevation, URA offer structural advantages [2], particularly for traditional direction of arrival (DoA) algorithms like 2D MUSIC or 2D Estimation of signal parameters via rotational invariance techniques (ESPRIT). However, a critical limitation arises when the final objective is precise localization (positioning) rather than just direction finding. While these algorithms can yield accurate angular estimates under a far-field (FF) plane-wave assumption, the subsequent conversion of these DoAs into a physical position is inherently unreliable for sources in the radiative NF or in the transition region.

Among the array processing techniques for DoA estimation, the MUSIC algorithm, a subspace-based method, is renowned for its high-resolution capabilities under ideal conditions [3]. However, MUSIC's primary drawback is its significant computational complexity, especially when applied to 2D DoA estimation (e.g., azimuth and elevation using URAs). This complexity stems from two main stages: the eigenvalue decomposition (EVD) or singular value decomposition (SVD) of the received signal's covariance matrix, typically scaling as $O(M^3)$ where M is the total number of array elements, and, often the exhaustive 2D peak search, which is the most demanding step. across the 2D spatial pseudospectrum [4,5]. This computational burden hinders the deployment of standard MUSIC in real-time applications or systems with constrained processing resources [6].

Several strategies have been proposed to mitigate the computational cost of the MUSIC peak search. Adaptive grid search techniques, often employing a zoom-in approach, aim to reduce the number of high-resolution evaluations by focusing computational effort on promising angular regions identified in an initial search for greater granularity [5,7]. While reducing the average complexity, these methods remain search-based and depend on the reliability of the initial, greater granularity detection. As a low-complexity benchmark, conventional beamforming based on the discrete fourier transform (DFT) offers computational complexity $O(M^2)$ but suffers from inherently poor angular resolution compared to subspace methods [8].

Geometric approaches that exploit the specific structure of the array, such as decomposing the URA response into contributions from virtual linear arrays [9], can lead to analytical or semi-analytical solutions, potentially eliminating the need for a 2D search entirely. The position estimation using circle and hyperbola (PEACH) approach falls into this category [10]. Techniques involving spatial interpolation of the greater granularity MUSIC pseudospectrum using bicubic interpolation have also been considered as a means to refine peak locations, and it is necessary to analyze the levels of the greater granularity and refined grids to ensure accurate peak capture.

Other advanced strategies, including search-free subspace methods like Root-MUSIC or ESPRIT adapted for URAs [11], and data-driven deep learning approaches [12], represent further avenues but often entail different complexities or requirements. Furthermore, recent advanced techniques based on tensor network decompositions, such as tensor train decomposition (TTD), have been proposed to leverage the multidimensional structure of signals from planar arrays, showing promise for high-accuracy angle estimation in complex multiple-input and multiple-output (MIMO) radar scenarios [13].

It is noteworthy that search-free subspace methods, such as 2D- ESPRIT and Root-MUSIC, are prominent low-complexity alternatives to MUSIC, with ESPRIT being particularly relevant for planar arrays [11]. In this study, we have tested these methods within our comparative analysis to evaluate their performance in the NF localization problem addressed herein, despite a fundamental mismatch. These algorithms are predicated on a FF, plane-wave assumption, which presumes both constant signal amplitude and a linear phase progression across the array elements, assumptions recently contrasted by data-driven deep learning approaches [12]. Our NF scenario directly violates these premises, as the spherical wavefront results in a non-linear phase, while the distance-dependent path loss ($1/d$) generates significant amplitude variation across the array. This mismatch invalidates the rotational invariance property essential for ESPRIT and the single-variable polynomial structure of Root-MUSIC, leading to severe performance degradation. Consequently, while we include them as baselines to highlight the impact of the model mismatch, our primary comparison focuses on methods that are inherently compatible with or adaptable to the more accurate NF model required for this scenario.

The demand for computationally efficient localization algorithms is increasingly critical in ISAC systems, motivating a comprehensive investigation of the performance–complexity trade-off among available techniques. In such paradigms, sensing and communication functions must share hardware and spectrum, making computational efficiency essential [14]. This integration promotes the extraction of sensing information from signals already present in the communication framework—such as pilot sequences—thus avoiding the need for dedicated sensing waveforms. This paper specifically addresses the challenge of 2D localization (estimating Cartesian (x, y) coordinates) of a single source confined to the ground plane ($z = 0$) using an elevated URA (e.g., mounted on a building rooftop), evaluating the inherent trade-offs between estimation accuracy and computational complexity, particularly for potential ISAC applications. It is crucial to distinguish between DoA estimation, which traditionally seeks to determine the azimuth and elevation angles of a source under a FF assumption, and direct position estimation (*i.e.*, localization), which aims to determine the source's exact Cartesian coordinates. This study focuses on the latter, directly estimating the (x, y) position. Consequently, the system model and the steering vector must be explicitly parameterized by these spatial coordinates rather than by azimuth and elevated angles. This choice deliberately frames the problem within a NF context, where the spherical curvature of the wavefront is significant, making this formulation essential for solving the direct localization problem addressed in this research.

The elevated geometry creates a specific relationship between the source's Cartesian coordinates and the observed signal parameters, which, in the context of NF localization, are the path-dependent phase and amplitude at each antenna element. This NF formulation is intentional. While the Fraunhofer distance often delineates the FF, this criterion is insufficient for localization tasks, where the wavefront curvature

ignored in the FF is precisely the source of range information essential for direct positioning [15,16]. Consequently, this work relies on a more accurate spherical-wave model, leveraging properties of the radiative NF that are critical in modern large-aperture systems [17].

To quantitatively evaluate the performance-complexity trade-offs, this work establishes three key benchmarks: (i) the Cramér–Rao Bound (CRB), representing the theoretical limit of estimation accuracy; (ii) the standard MUSIC NF algorithm with a fine grid search, serving as the high-resolution, high-complexity baseline; and (iii) DFT NF Beamforming, acting as the low-resolution, low-complexity baseline. Against these references, we evaluate several promising low-complexity strategies: a geometric decomposition approach (PEACH), orthogonal matching pursuit (OMP), and two refinement techniques based on a standard MUSIC-NF spectrum (Adaptive Grid and Bicubic Interpolation). The novelty lies in the specific application to an elevated URA for ISAC systems and the direct, quantitative comparison of these specific methods under a unified simulation framework.

2. Methods

In this work, we employ Monte Carlo simulations to evaluate and compare the performance of various NF localization strategies. Each Monte Carlo trial proceeds as follows:

(1) Generate a synthetic received signal at an elevated URA under free-space propagation for a single target located at a random but non-overlapping position within the surveillance region.
(2) Add white Gaussian noise corresponding to a specified SNR.
(3) The localization is estimated by each selected method.
(4) When applicable, a refined method is used to improve the estimation.
(5) These methods are evaluated in terms of localization accuracy RMSE and execution time per trial, varying the SNR and the number of snapshots L.

All simulations were implemented in MATLAB R2023b on a standard desktop computer. Execution time for each method was measured using MATLAB's tic/toc functions to assess computational complexity. The key parameters used in our experiments are summarized in Table 1. Wherever additional parameters are method-specific they are indicated in the text.

For each SNR value and each number of snapshots L, the procedure is repeated for every method for N_{trials} independent trials, and the RMSE of the estimated position is averaged over all trials.

Performance Metrics

Localization accuracy: RMSE of the estimated target position, averaged over all Monte Carlo trials.

Computational complexity: Average execution time measured per trial; comparisons are made relative to the benchmarks and other methods.

Table 1. Simulation parameters.

Parameter	Value
Scenario and Array Parameters	
Operating Frequency (f_c)	15 GHz
Wavelength (λ)	20 mm
URA Size (M)	8×8 elements (M = 64)
Element Spacing	$\lambda/2$
Antenna Height ($\bar{z}$)	20 m
User Surveillance Area (x, y)	$[-40, 40]$ m, $[15, 45]$ m
Signal and Simulation Parameters	
Number of Snapshots (L)	[50, 100, 200, 300, 500]
SNR Range	-5 to 20 dB (in 5 dB steps)
Monte Carlo Trials (N_{trials})	1000
Algorithm-Specific Grid Parameters	
Grid granulometry G_f	600×600 points
PEACH 1D Search Points G_{peach}	100 (hyperbola) + 200 (circle)
Initial Grid to refine G_c	200×200 points
Window size to refine	1×1 (m) around the coarse peak
Grid points inside the window G_w	$\approx 7 \times 17$ points

3. System model

In this research, we examine the accurate localization of a single user within a specified area using an elevated antenna array, as depicted in Figure 1. The planar array is installed on a building's rooftop, emulating a realistic urban base station scenario. This elevated geometry is crucial, as it creates the geometric diversity necessary for direct position estimation. A central premise of this work is the distinction between traditional DoA estimation and direct position estimation (*i.e.*, localization). While DoA methods seek to find FF angles (azimuth and elevation), our goal is to directly estimate the source's exact Cartesian coordinates (x, y) on the ground plane. This objective mandates a physical model sensitive to the source's range, not just its direction. This critical range information is physically encoded in the spherical curvature of the propagating wavefront, a characteristic that is only significant in the radiative NF.

Consequently, a conventional FF model, which assumes planar wavefronts, is fundamentally unsuitable for this task. The plane-wave approximation inherently discards wavefront curvature, which is precisely the carrier of the range information essential for direct positioning. The formal boundary between these regimes is often cited as the Fraunhofer distance, typically defined as $2D^2/\lambda$, where D is the largest dimension of the array and λ is the wavelength [18]. However, this criterion was historically established to ensure minimal phase error for FF antenna pattern measurements, not for localization tasks. A source can be beyond this distance, yet still be too close for the plane-wave assumption to be effective

for positioning, as the very curvature the criterion allows one to ignore is what enables localization [15,16]. This nuanced understanding is increasingly critical in modern systems featuring large apertures, where the radiative NF extends over considerable distances and its properties are intentionally exploited for high-resolution sensing.

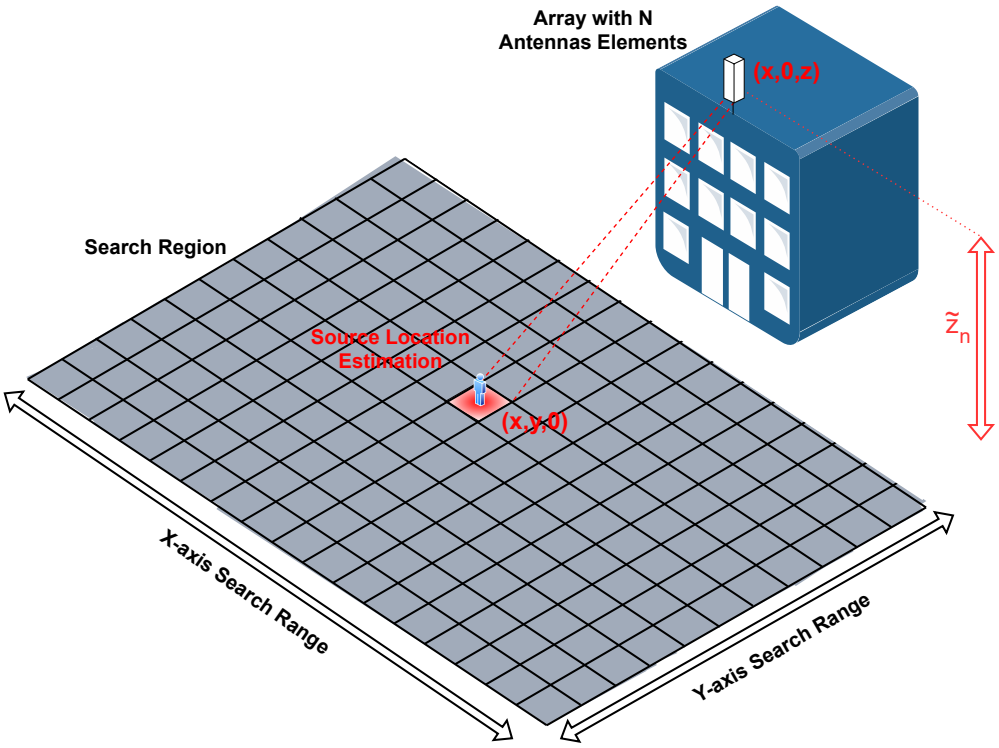

Figure 1. Design of elevated planar array antennas with users located on a delimited ground-level xy-plane. The user position vector is denoted as $\mathbf{u}_k = [x_k, y_k]^T$, located on the ground plane ($z = 0$).

Therefore, to solve the direct localization problem, the system model and the steering vector must be explicitly parameterized by the spatial coordinates (x,y). This choice deliberately frames the problem within a NF context, making the formulation essential for this research. The geometry of the system is defined by the coordinates of the user source and the antenna elements. The antenna array is assumed to lie on the xz-plane, while the user is on the ground-level xy-plane. The respective coordinates are given by:

$$\mathbf{u}_k = [x_k, y_k, 0]^{\mathrm{T}} \quad \text{and} \quad \mathbf{p}_m = [x_m, 0, z_m]^{\mathrm{T}}, \quad m = 1, \ldots, M \tag{1}$$

where $\mathbf{u}_k$ denotes the position of the k-th user and $\mathbf{p}_m$ specifies the location of the m-th antenna element and $(\cdot)^{\mathrm{T}}$ denotes the transpose operator. For an elevated URA, we define $\tilde{z}_m$ as the average height of the antenna configuration.

The received signal vector at the array, $\mathbf{y}(t)$, is modeled as:

$$\mathbf{y}(t) = e^{j\psi_0}\mathbf{a}(\mathbf{u}_k)s(t) + \mathbf{n}(t), \tag{2}$$

where $s(t)$ represents a known pilot sequence transmitted by the user for purposes such as channel estimation or synchronization [14], $\mathbf{n}(t)$ is the additive white Gaussian noise vector with variance σ_n^2 and ψ_0 is a differential phase offset. By leveraging this existing communication signal for localization, our

model explicitly embodies a key principle of ISAC, the dual use of signals for both communication and sensing tasks.

The core of this model is the steering vector, $\mathbf{a}(\mathbf{u}_k)$, which must be consistent with our NF formulation. It explicitly depends on the user's Cartesian coordinates by incorporating both the free-space path loss factor $\lambda/(4\pi)$ and the spherical wavefront phase curvature [19–21]. It is expressed as:

$$\mathbf{a}(\mathbf{u}_k) = \frac{\lambda}{4\pi}\left[\frac{1}{d_1}, \frac{e^{-j\frac{2\pi}{\lambda}(d_2-d_1)}}{d_2}, \ldots, \frac{e^{-j\frac{2\pi}{\lambda}(d_M-d_1)}}{d_M}\right]^{\mathrm{T}}, \tag{3}$$

where λ is the carrier wavelength and d_m is the Euclidean distance between the user at $\mathbf{u}_k$ and the m-th antenna element at $\mathbf{p}_m$. This model assumes a pure LOS propagation scenario, which is a suitable approximation for elevated antenna deployments in urban environments, especially at higher frequencies where the LOS component is dominant.

4. Performance and complexity benchmarks

The following sections detail the algorithms evaluated in this study. The analysis is structured around a set of established benchmarks that define the boundaries of the performance-complexity trade-off space. We begin by describing these benchmarks: CRB as the theoretical performance limit, the standard MUSIC NF algorithm as the high-resolution baseline, and DFT NF beamforming as the low-complexity baseline. Subsequently, we describe the promising low-complexity strategies evaluated against these references, including refinement techniques, a geometric approach (PEACH-MUSIC), and a OMP.

4.1. Derivation of the Cramér-Rao bound for 2D localization

The CRB establishes the theoretical lower bound for the variance of any unbiased estimator and is obtained from the inverse of the fisher information matrix (FIM), $\mathbf{J}(\mathbf{u}_k)$, where σ_n^2 denotes the noise variance. Based on the FIM, we present steps for deriving the CRB for the 2D position vector $\mathbf{u}_k = [x_k, y_k]^{\mathrm{T}}$, where x_k and y_k represent the Cartesian ground-plane coordinates of the k-th user. We begin by defining the complete received signal model in matrix form. Let $\mathbf{Y}$ be the $M \times L$ matrix containing all L snapshots of the received signal across the M antenna elements. This matrix can be expressed as: the covariance matrix of the received data must be estimated and decomposed to extract $\mathbf{U}_s$, operations that already impose substantial computational overhead. During the iterative search, the algorithm evaluates correlations for each candidate position, requiring repeated generation and normalization of steering vectors, which further compounds the overall computational cost

$$\mathbf{Y} = \mathbf{a}(\mathbf{u}_k)\mathbf{s}(t)^{\mathrm{T}} + \mathbf{N}, \tag{4}$$

where $\mathbf{a}(\mathbf{u}_k)$ is the $M \times 1$ NF steering vector defined in Equation (3), $\mathbf{s}(t)$ is the $L \times 1$ vector of transmitted pilot signals $s_l(t)$, and $\mathbf{N}$ is the $M \times L$ matrix of additive white Gaussian noise (AWGN). Each column of $\mathbf{N}$ is an independent realization of a complex Gaussian random vector with covariance $\sigma_n^2\mathbf{I}$.

The probability density function (PDF), $p(\cdot)$, of the noise matrix $\mathbf{N}$ is given by:

$$p(\mathbf{N}) = \frac{1}{(\pi\sigma_n^2)^{ML}} \exp\left(-\frac{1}{\sigma_n^2}\mathrm{Tr}(\mathbf{N}\mathbf{N}^H)\right), \tag{5}$$

where $\mathrm{Tr}(\cdot)$ denotes the trace of a matrix and $(\cdot)^H$ is the conjugate transpose. By substituting $\mathbf{N} = \mathbf{Y} - \mathbf{a}(\mathbf{u}_k)\mathbf{s}(t)^{\mathrm{T}}$, we obtain the likelihood function of $\mathbf{Y}$ given the position $\mathbf{u}_k$. Taking the natural logarithm yields the log-likelihood function:

$$\ln p(\mathbf{Y}|\mathbf{u}_k) = -ML\ln(\pi\sigma_n^2) - \frac{1}{\sigma_n^2}\mathrm{Tr}\left((\mathbf{Y} - \mathbf{a}(\mathbf{u}_k)\mathbf{s}(t)^{\mathrm{T}})(\mathbf{Y} - \mathbf{a}(\mathbf{u}_k)\mathbf{s}(t)^{\mathrm{T}})^H\right), \tag{6}$$

the trace term expands as follows:

$$\ln p(\mathbf{Y} \mid \mathbf{u}_k) = -ML\ln(\pi\sigma_n^2) - \frac{1}{\sigma_n^2}\sum_{l=1}^{L} \|\mathbf{y}(t) - \mathbf{a}(\mathbf{u}_k)s_l(t)\|^2 \tag{7}$$

Defining FIM as the expected value of the negative second derivative of the log-likelihood function with respect to parameter vector $\mathbf{u}_k$:

$$\mathbf{J}(\mathbf{u}_k) = -\mathbb{E}\left[\frac{\partial^2 \ln \mathrm{p}(\mathbf{Y} \mid \mathbf{u}_k)}{\partial \mathbf{u}_k \partial \mathbf{u}_k^{\mathrm{T}}}\right] \tag{8}$$

To compute the second derivative, we take the gradient of the steering vector $\mathbf{a}(\mathbf{u}_k)$ with respect to $\mathbf{u}_k$. The steering vector is given as in Equation (3), with $d_m = \sqrt{(x-x_m)^2 + y^2 + z_m^2}$. The gradient of $\mathbf{a}(\mathbf{u}_k)$ with respect to x and y requires FIM computation. For the x-component, the gradient is given by:

$$\frac{\partial \mathbf{a}(\mathbf{u}_k)_m}{\partial x} = \frac{\lambda}{4\pi} e^{-j\frac{2\pi}{\lambda}(d_m - d_1)} \left(-\frac{\delta_m}{d_m^3} - j\frac{2\pi}{\lambda}\left(\frac{\delta_m}{d_m^2} - \frac{\delta_1}{d_1 d_m}\right)\right) \tag{9}$$

where $\delta_m = x - x_m$ and $\delta_1 = x - x_1$; analogously, one can compute gradient fo the y-component the gradient is:

$$\frac{\partial \mathbf{a}(\mathbf{u}_k)_m}{\partial y} = \frac{\lambda}{4\pi} y e^{-j\frac{2\pi}{\lambda}(d_m - d_1)} \left(-\frac{1}{d_m^3} - j\frac{2\pi}{\lambda}\left(\frac{1}{d_m^2} - \frac{1}{d_1 d_m}\right)\right) \tag{10}$$

To compute the FIM $\mathbf{J}(\mathbf{u}_k)$, we take the expectation of the outer product of these gradients, resulting: For J_{xx} , we compute:

$$J_{xx} = \mathbb{E}\left[\frac{\partial \ln p(\mathbf{Y} \mid \mathbf{u}_k)}{\partial x}\left(\frac{\partial \ln p(\mathbf{Y} \mid \mathbf{u}_k)}{\partial x}\right)^H\right] \tag{11}$$

Substituting the derivative of $\mathbf{a}(\mathbf{u}_k)$ with respect to x, we have:

$$J_{xx} = P_{\mathrm{norm}} \sum_{m=1}^{M} \left[\left(\frac{\delta_m}{d_m^3}\right)^2 + \left(\frac{2\pi}{\lambda}\left(\frac{\delta_m}{d_m^2} - \frac{\delta_1}{d_1 d_m}\right)\right)^2\right] \tag{12}$$

Similarly, for J_{yy} and J_{xy} we have:

$$J_{yy} = P_{\text{norm}}\, y^2 \sum_{m=1}^{M} \left[\frac{1}{d_m^6} + \left(\frac{2\pi}{\lambda} \left(\frac{1}{d_m^2} - \frac{1}{d_1 d_m} \right) \right)^2 \right] \tag{13}$$

Finally, for the cross term J_{xy}, we compute:

$$J_{xy} = P_{\text{norm}}\, y \sum_{m=1}^{M} \left[\frac{\delta_m}{d_m^6} + \left(\frac{2\pi}{\lambda} \right)^2 \left(\frac{\delta_m}{d_m^2} - \frac{\delta_1}{d_1 d_m} \right) \left(\frac{1}{d_m^2} + \frac{1}{d_1 d_m} \right) \right] \tag{14}$$

where $P_{\text{norm}} = L \left(\frac{|s|\lambda}{\sqrt{2}\pi\sigma_n} \right)^2$, $|s|$ is the magnitude of the transmitted pilot signal, assumed to be constant. The CRB for the x and y coordinates are the diagonal elements of the inverse FIM, calculated as:

$$\text{CRB}(x) = [\mathbf{J}^{-1}]_{11} = \frac{J_{yy}}{J_{xx}J_{yy} - J_{xy}^2} \tag{15}$$

$$\text{CRB}(y) = [\mathbf{J}^{-1}]_{22} = \frac{J_{xx}}{J_{xx}J_{yy} - J_{xy}^2} \tag{16}$$

4.2. Dictionary generation for search-based methods

Several of the evaluated localization algorithms, including MUSIC, DFT NF and OMP NF, rely on a search-based approach to find the user's position. This process involves comparing the received signal against a set of theoretical signal responses, known as a dictionary. The dictionary, $\mathbf{D}$, is an $M \times G$ matrix where each column represents a normalized steering vector corresponding to a candidate position on a discretized search grid. The quality of this dictionary is fundamental to the accuracy of the localization. In this work, we consider two distinct physical models for constructing these dictionaries: a NF model and a FF model.

4.2.1. Near-field dictionary

The foundation for all search-based methods is a set of candidate steering vectors generated for a discretized Cartesian grid near-field dictionary, $\mathbf{D}_{\text{NF}}$, with g_x points along the x-axis and g_y points along the y-axis, resulting in a total of $G = g_x \cdot g_y$ candidate positions $\mathbf{u}_i = [x_i, y_i, 0]^{\text{T}}$. The unnormalized near-field steering vector $\mathbf{a}(\mathbf{u}_i)$, as defined in Equation (3), is the primary component as it preserves the complete physical information of the spherical wavefront, including both the characteristic amplitude decay and phase curvature. Techniques such as MUSIC NF and DFT NF utilize this unnormalized vector directly.

Conversely, certain algorithms like OMP NF require a normalized dictionary to perform comparisons based on structural similarity, independent of signal strength. For these specific methods, the normalized near-field dictionary, $\mathbf{D}_{\text{NF}}^{\text{norm}}$, is constructed. Each column $\mathbf{d}_i$ is the unit-norm version of the corresponding steering vector $\mathbf{a}(\mathbf{u}_i)$ from Equation (3):

$$\mathbf{d}_i = \frac{\mathbf{a}(\mathbf{u}_i)}{||\mathbf{a}(\mathbf{u}_i)||_2}, \quad \text{for } i = 1, \ldots, G. \tag{17}$$

This dictionary is parameterized directly by the Cartesian coordinates (x, y), and each column contains the characteristic amplitude decay and phase curvature of a spherical wavefront, making it

suitable for direct localization.

4.2.2. Far-field dictionary

For comparison and to evaluate the performance of traditional DoA-based algorithms, we also define a FF (plane wave) dictionary. This model assumes the source is sufficiently distant such that the wavefront arriving at the array is planar. The steering vector is no longer parameterized by Cartesian coordinates directly, but by the direction of arrival, typically expressed in terms of azimuth ϕ and elevation θ.

For a URA positioned on the xz-plane, the FF steering vector, $\mathbf{a}_{\text{FF}}$, for a signal arriving from (θ, ϕ) is given by:

$$\mathbf{a}_{\text{FF}}(\theta,\phi) = \frac{1}{\sqrt{M}}[e^{-j\frac{2\pi}{\lambda}(x_1 \sin\theta\cos\phi + z_1\cos\theta)}, \ldots, e^{-j\frac{2\pi}{\lambda}(x_M \sin\theta\cos\phi + z_M\cos\theta)}]^T, \tag{18}$$

where $(x_m, 0, z_m)$ are the coordinates of the m-th antenna element. Note that this model assumes uniform amplitude across all elements, neglecting path loss differences.

To create a FF dictionary, $\mathbf{D}_{\text{FF}}$, over the same Cartesian grid of G positions $\mathbf{u}_i = [x_i, y_i, 0]^T$, we must first convert each candidate position into its corresponding DoA angles (θ_i, ϕ_i). Given the elevated array geometry with an average height of $\bar{z}$, this geometric conversion is:

$$\text{Range,} \qquad r_i = \sqrt{x_i^2 + y_i^2 + \bar{z}^2} \tag{19}$$

$$\text{Elevation,} \quad \theta_i = \arccos\left(\frac{\bar{z}}{r_i}\right) \tag{20}$$

$$\text{Azimuth,} \qquad \phi_i = \arctan 2(y_i, x_i) \tag{21}$$

Each column of the FF dictionary is then constructed by substituting these calculated angles into the FF steering vector model:

$$\mathbf{d}_i = \mathbf{a}_{\text{FF}}(\theta_i, \phi_i), \quad \text{for } i = 1, \ldots, G. \tag{22}$$

This dictionary allows us to evaluate the performance degradation that occurs when FF assumptions are incorrectly applied to a NF localization problem.

It is worth noting that while we tested search-free methods like Root-MUSIC as FF baselines, the algorithm is fundamentally inoperable in our NF model. Root-MUSIC requires a Uniform Linear Array (ULA) for its polynomial rooting formulation and assumes a FF plane-wave model with constant amplitude and linear phase progression. Our elevated URA and NF spherical wavefront violate these premises, leading to its inoperability. To demonstrate this incompatibility, we ran 2D MUSIC tests using the FF dictionary, with the same number of points while maintaining the same level of complexity, as evidenced by the high error bound observed in our numerical results.

4.3. Multiple signal classification (MUSIC) for NF localization

The MUSIC NF (Algorithm 1) [22–24] is a high-resolution, subspace-based technique renowned for estimating the 2D position via DoA of signals incident on an antenna array, under ideal conditions. However, its performance can degrade significantly when these conditions are not met, as detailed in the following section. The algorithm computes the pseudospectrum by sampling it over a discrete x, y-grid, a

process that introduces a greater granularity, as the true peak may lie between the sampled grid points. A critical distinction arises from the physical model used to generate the dictionary's steering vectors. The choice between a NF and a FF model defines the applicability or operability of the algorithm for localization.

For direct position estimation, as required in this work, the MUSIC NF formulation is the appropriate choice. This approach, enabled by the spatial diversity of the planar array, performs the search directly over a Cartesian grid of candidate positions (x,y) and utilizes the NF dictionary, $\mathbf{D}_{NF}$, described in Section 4.2. Each column in this dictionary correctly models the spherical wavefront, preserving the range-dependent information essential for accurate localization. Conversely, the conventional FF MUSIC (2D MUSIC) operates by searching over a grid of angles (θ,ϕ) using a FF dictionary, $\mathbf{D}_{FF}$. While the array's planar structure provides the necessary 2D aperture to resolve both azimuth and elevation, this angular search is only effective if the incoming signal is accurately approximated by a plane wave. As established in this work, even sources beyond the Fraunhofer distance may not satisfy this condition for localization, making the approach inherently suboptimal as it discards crucial wavefront curvature information.

Although MUSIC NF offers high detection resolution, its primary drawback remains its significant computational complexity. While this computational burden is a primary disadvantage, a detailed quantitative analysis of its asymptotic complexity, benchmarked against the other strategies evaluated in this work, will be presented in Section 4.11. The cost of this search is strongly influenced by the grid resolution. While refining the search grid increases localization accuracy by enabling the detection of peaks that might lie between the originally sampled points, this refinement comes at a cost, as the total number of evaluations rises approximately with the square of the grid dimension. For example, a 40×40 grid requires $1,600$ evaluations, whereas a 100×100 grid would require $10,000$ evaluations, leading to a considerably higher execution time. Therefore, a trade-off exists between estimation accuracy and computation time, and the grid size must be chosen considering the specific application requirements. The operational steps of the algorithm are summarized in Algorithm 1.

Algorithm 1 MUSIC NF

Input: $\mathbf{Y}$; array geometry, grid parameters-$\mathbf{D}_{\text{NF}}$; λ; K
$L \leftarrow$ number of columns in $\mathbf{Y}$
Compute the mean covariance matrix $\mathbf{R}$
  $\mathbf{R} \leftarrow \frac{1}{L}\mathbf{Y}\mathbf{Y}^H$
Perform eigenvalue decomposition of $\mathbf{R}$
  $(\mathbf{U},\Lambda) \leftarrow \text{eig}(\mathbf{R})$
Construct the noise subspace $\mathbf{U}_n$
Let $K = 1$ (single source assumption)
  $\mathbf{U}_n \leftarrow$ eigenvec of the smallest eigenvalue $(M-K)$
for each $\mathbf{u}_i$ in the grid **do**
  Compute steering vector candidate $\mathbf{a}(\mathbf{u}_i)$;
  Evaluate $P(x_i,y_i) \leftarrow \frac{1}{\mathbf{a}_i^H\mathbf{U}_n\mathbf{U}_n^H\mathbf{a}_i}$
end for
Output: $\hat{\mathbf{u}_k}(\hat{x},\hat{y}) = \arg\max P(x_i,y_i)$;

4.3.1. Scenarios that degrade MUSIC

Under ideal circumstances, the MUSIC algorithm is well known for its high-resolution capabilities; however, in more realistic situations, its performance can suffer considerably. Low SNR, a small number of snapshots, and model incompatibilities such as array imperfections and mutual coupling pose specific challenges to its robustness.

At low SNR regimes, the separation between the signal and noise subspaces becomes less distinct, which may lead to erroneous identification of the signal subspace and consequently to poor localization accuracy. The eigenvalue spread of the covariance matrix under noise-dominated conditions can mask the presence of weak sources, thereby increasing the estimation variance [25]. This effect is particularly pronounced when the source signal power is close to or below the noise floor, as also observed in practical radar and wireless communication contexts.

Additionally, the number of available temporal snapshots has a direct impact on the reliability of the covariance matrix estimation. With few snapshots, the sample covariance matrix poorly approximates the true covariance, increasing estimation bias and variance. This sensitivity is well documented in [4], where it is shown that MUSIC requires a sufficiently large number of observations to maintain its subspace orthogonality property. In ISAC scenarios where sensing resources are shared with communication, the number of snapshots may be constrained, aggravating this limitation.

Furthermore, model mismatches such as calibration errors, array position inaccuracies, and mutual coupling between adjacent antenna elements may distort the array manifold, breaking the assumed orthogonality between signal and noise subspaces. As a result, spurious peaks can appear in the pseudospectrum, leading to biased localization estimates. This phenomenon has been reported in several studies on practical array implementations [4], highlighting the importance of robust array calibration and compensation techniques.

In summary, while computational complexity is a key barrier to real-time deployment of MUSIC, its robustness under adverse conditions is equally critical. These degradation factors motivate the investigation of hybrid approaches, such as PEACH-MUSIC and interpolation-assisted refinements, which may alleviate sensitivity to noise and model errors while maintaining reduced complexity.

4.4. Technique to reduce complexity

To address the computational complexity associated with the two-dimensional MUSIC pseudospectrum, we evaluate several promising low-complexity strategies, including Adaptive Grid Search, Bicubic Interpolation, PEACH-MUSIC, and OMP NF. These strategies are benchmarked against established methods, such as the standard MUSIC uniform search and DFT NF beamforming, as well as the theoretical CRB to assess their ultimate performance limits. The peak-finding approaches investigated include the following:

(1) Bicubic Interpolation: This technique employs an initial coarse grid search to identify a smaller region of interest, subsequently enhancing resolution within this region using bicubic interpolation.
(2) Adaptive Grid Search (Zoom-in): In the same way, initially conducting a low-complexity coarse search identifies a smaller region of interest, followed by a refined search performed exclusively within this targeted area.
(3) PEACH-MUSIC: Using innovative geometric decomposition, this approach circumvents the

simultaneous handling of all antenna elements, significantly reducing computational demands.

The detailed operational principles and implementations of these methods are elaborated in the following sections.

4.5. MUSIC with bicubic interpolation

Our goal is to apply bicubic interpolation to the MUSIC pseudospectrum in order to improve the accuracy without the additional computational cost caused by grid refinement [26]. Coarse grids may limit interpolation effectiveness, preventing any meaningful improvement in accuracy. This limitation should be noted.

The primary advantage of the interpolation-based method lies in the substantial reduction in computational demand. The initial MUSIC spectral evaluation is performed on a mere $200 \times 200 = 40,000$ grid points. This represents a dramatic decrease of over 90% in the number of points compared to the $360,000$ points needed by the standard fine-grid MUSIC to achieve similar accuracy. Although bicubic interpolation introduces its own computational overhead, this is significantly less than performing a full MUSIC search on a correspondingly dense grid. Consequently, a considerable overall saving in execution time is achieved while preserving localization precision, as will be further detailed.

This initial finding is highly promising, showcasing the significant potential of employing bicubic interpolation to optimize the 2D MUSIC algorithm for high-accuracy localization with reduced computational resources. The robustness and performance benefits of this MUSIC with bicubic interpolation approach will be further rigorously evaluated under a variety of operational conditions and diverse scenarios in the subsequent numerical results section. We will not perform interpolation on the entire pseudospectrum. After finding the peak in the greater granularity pseudospectrum, we will use windowing in the same manner as detailed in adaptive grid search. A detailed analysis of this method's computational complexity is provided in Section 4.11.

4.6. MUSIC with Adaptive Grid Search (Zoom-in)

The Adaptive Grid Search, or "Zoom-in" method, described in Algorithm 2, aims to improve localization accuracy while reducing computational complexity by concentrating computational effort in a localized search region. Starting from an initial greater granularity estimate (x_c, y_c), a refined search is conducted within a smaller window centered at (x_c, y_c).

The refinement region is typically defined as a square area covering $\pm W_x$ and $\pm W_y$ meters along the x and y axes, respectively:

$$G_w = \{(x,y) : |x - x_c| \leq W_x,\ |y - y_c| \leq W_y\} \tag{23}$$

Within this region, the MUSIC pseudospectrum is evaluated over a finer granularity grid, and the final estimate is obtained as:

$$(\hat{x}, \hat{y}) = \arg \max_{x,y \in G_w} P_{\text{MUSIC}}(x,y) \tag{24}$$

Although the refinement search remains exhaustive inside the window, it involves substantially fewer grid points than a global fine-grid search. The choice of W_x and W_y balances the risk of missing the true peak (if the window is too narrow) against unnecessary computational cost (if the window is too wide).

The computational complexity of this approach is formally analyzed in Section 4.11.

Algorithm 2 Adaptive Grid Search (Zoom-in)

Input: $\mathbf{Y}$; array geometry; grid parameters-$\mathbf{D}_{\mathrm{NF}}$; W; λ; K.
1. Coarse Search Stage
Perform MUSIC NF algorithm (as in Algorithm 1) on the coarse grid.
Let (x_c, y_c) be the resulting coarse position estimate.
2. Refined Search Stage (Zoom-in)
Define a refined search region G_w as a window of size W around (x_c, y_c).
Generate a fine grid of candidate positions within G_w. Re-compute pseudospectrum only within the refined region
$\mathbf{U}_n \leftarrow$ Noise subspace from $\mathbf{Y}$ (can be reused from coarse stage).
for each $\mathbf{u}_i$ in the grid **do**
    Compute steering vector candidate $\mathbf{a}(\mathbf{u}_i)$;
    Evaluate $P_{\text{fine}}(x_i, y_i) \leftarrow \frac{1}{\mathbf{a}_i^H \mathbf{U}_n \mathbf{U}_n^H \mathbf{a}_i}$
end for
3. Final Estimation
Output: $\hat{\mathbf{u}}_k(\hat{x}, \hat{y}) = \arg\max P_{\text{fine}}(x_i, y_i)$;

4.7. Position estimation algorithm using circles and hyperbolas (PEACH-MUSIC)

The PEACH-MUSIC algorithm leverages the geometric structure of the URA by conceptually decomposing it into two orthogonal one-dimensional SAs: a horizontal SA (a single row) and a vertical SA (a single column) [10]. By processing the signals from these two SAs independently, the 2D search problem can be reduced to a more efficient analytical solution.

The core principle is that the pseudospectrum generated by the MUSIC method using a horizontal SA forms hyperbolic detection regions in the xy-plane. Conversely, a vertical SA yields circular regions [10]. The intersection between these two geometric regions enables the precise localization of a single user. Specifically, the vertical SA defines a circular region in the horizontal plane given by:

$$x^2 + y^2 = d_{xy}^2, \tag{25}$$

where d_{xy} corresponds to the radius directly estimated from the pseudospectrum generated by the vertical SA. The horizontal SA, in contrast, generates hyperbolic regions characterized by the difference in distances, Δ, between the received signals at its endpoints, situated at symmetric positions $(-c, 0, z_a)$ and $(c, 0, z_a)$, c is the absolute x-coordinate of the symmetric endpoints of the horizontal SA:

$$|d_1 - d_2| = \Delta, \tag{26}$$

with the distances $d_{1,2}$ expressed as $d_{1,2} = \sqrt{(x \mp c)^2 + y^2 + z_a^2}$. The user's coordinates are then determined analytically by solving this system of equations formed by Equations (25) and (26), which yields:

$$x^2 = \frac{\Delta^2}{16c^2}[4(c^2 + d_{xy}^2 + z_a^2) - \Delta^2] \tag{27}$$

$$y^2 = d_{xy}^2 - x^2 \tag{28}$$

The correct signs for the coordinates are resolved through the peaks of the pseudospectrum, significantly decreasing computational complexity compared to an exhaustive 2D grid search.

Simplified One-Dimensional Search for Efficient Localization

This method further enhances computational efficiency by replacing an exhaustive 2D search with two independent 1D spectral searches. First, a 1D search is performed along the x-axis (assuming $(y = 0)$) using the horizontal SA's noise subspace to find the hyperbolic parameter (Δ). Second, another 1D search is conducted along the y-axis (assuming $(x = 0)$) using the vertical SA to estimate the radius (d_{xy}) of the circular region. The user's position is then computed analytically from these two parameters, with the sign ambiguity resolved using the peak location from the horizontal search. This targeted approach significantly reduces computation by avoiding a full two-dimensional scan, as detailed in Algorithm 3. A formal complexity analysis for this algorithm is detailed in Section 4.11.

Algorithm 3 PEACH-MUSIC

Input: $\mathbf{Y}$, array geometry, grid parameters PEACH.
1. Generate noise subspaces for horizontal and vertical SAs:
$\mathbf{Y}_h \leftarrow$ Select data from the horizontal SA of $\mathbf{Y}$.
$\mathbf{R}_h \leftarrow \frac{1}{L}\mathbf{Y}_h\mathbf{Y}_h^H$.
$\mathbf{U}_h \leftarrow$ Extract noise subspace from the eigendecomposition of $\mathbf{R}_h$.
$\mathbf{Y}_v \leftarrow$ Select data from the vertical SA of $\mathbf{Y}$.
$\mathbf{R}_v \leftarrow \frac{1}{L}\mathbf{Y}_v\mathbf{Y}_v^H$.
$\mathbf{U}_v \leftarrow$ Extract noise subspace from the eigendecomposition of $\mathbf{R}_v$.
2. Estimate geometric parameters via 1D MUSIC searches
$\Delta \leftarrow$ Compute hyperbolic parameter from $\mathbf{U}_h$, Equation (26).
$d_{xy} \leftarrow$ Compute circular radius from $\mathbf{U}_v$, Equation (25).
$x_{\text{sign}} \leftarrow$ Determine the sign of the x-coordinate from the peak of the horizontal.
3. Compute final position via analytical intersection
$x_{\text{abs}} \leftarrow$ Analytically compute the absolute value of x using Δ and d_{xy} (from Equation 27).
$\hat{y} \leftarrow \sqrt{d_{xy}^2 - x_{\text{abs}}^2}$.
$\hat{x} \leftarrow x_{\text{sign}} \cdot x_{\text{abs}}$.
Output: $\hat{\mathbf{u}}_k = [\hat{x}, \hat{y}]$.

4.8. Discrete Fourier transform (DFT) NF beamforming

The classical two-dimensional (2D) DFT beamformer provides a systematic scanning of a predefined NF dictionary, testing each candidate, to estimate the source position. The received signal, captured across the array elements, is then projected onto this steering vector. This projection yields the beamforming power output for that specific spatial coordinate. The process is repeated for all points across the entire dictionary, creating a power map of the search area. The final position estimate is determined by identifying the coordinates that yield the maximum beamforming power output on this map [27].

$$P_{\text{DFT}}(\mathbf{u}_i) = \frac{1}{L}\sum_{t=1}^{L}\left|\mathbf{a}(\mathbf{u}_i)^H\mathbf{y}(t)\right|^2$$

where $\mathbf{a}(\mathbf{u}_i)$ denotes the steering vector corresponding to position $i_{(x,y)}$, $\mathbf{y}(t)$ is the received signal vector at t, and L is the number of snapshots.

The estimated source position is obtained by locating the peak of the beamforming response:

$$(\hat{x},\hat{y}) = \arg\max_{x,y} P_{\mathrm{DFT}}(\mathbf{u}_i). \tag{29}$$

The steering vector $\mathbf{a}(\mathbf{u}_i)$ is computed according to the geometric model described in Equation (3), incorporating the distances between the user position and each array element. This operation is systematized in the algorithm 4. The computational complexity analysis for DFT NF is presented in Section 4.11.

Algorithm 4 DFT NF Beamforming

Input: $\mathbf{Y}$; array geometry; grid parameters; λ; K.
$L \leftarrow$ number of columns in $\mathbf{Y}$
1. Search over the Cartesian grid.
for each $\mathbf{u}_i$ in the grid **do**
  Compute steering vector candidate $\mathbf{a}(\mathbf{u}_i)$;
  Evaluate beamforming power by projecting the signal onto the steering vector
  $P_{\mathrm{DFT}}(\mathbf{u}_i) \leftarrow \frac{1}{L}\sum_{l=1}^{L} |\mathbf{a}(\mathbf{u}_i)^H \mathbf{y}(t_l)|^2$
end for
2. Estimate position as the peak of the beamforming response.
$(\hat{x},\hat{y}) \leftarrow \arg\max_{x,y} P_{\mathrm{DFT}}(\mathbf{u}_i)$ Equation (29)
Output: $\hat{\mathbf{u}_k} = [\hat{x},\hat{y}]$.

4.9. Compressive sensing approach: orthogonal matching pursuit (OMP) NF

OMP is a greedy iterative algorithm from the field of sparse signal recovery, which iteratively selects the dictionary column most correlated with the signal residual [28]. The core principle of OMP NF in the context of localization is that the signal subspace, $\mathbf{U}_s$, can be sparsely represented by a few columns from a large, overcomplete dictionary matrix—$\mathbf{D}_{\mathrm{NF}}^{\mathrm{norm}}$. Each column in this dictionary corresponds to a theoretical steering vector for a specific location on a discretized search grid. The goal is to identify the columns that best represents the observed signal, thereby determining the source's location. The localization problem can be formulated as finding a sparse coefficient vector, α, that solves:

$$\min ||\alpha||_0 \quad \text{subject to} \quad ||\mathbf{U}_s - \mathbf{D}_{\mathrm{NF}}^{\mathrm{norm}}\alpha||_2 \leq \varepsilon, \tag{30}$$

where $||\cdot||_0$ is the ℓ_0-norm (counting the non-zero elements), $\mathbf{U}_s$ is the $M \times 1$ principal eigenvector of the signal covariance matrix (*i.e.*, the signal subspace for a single source), and ε is a noise tolerance parameter. The dictionary $\mathbf{D}_{\mathrm{NF}}^{\mathrm{norm}}$ is an $M \times G$ matrix where each column is a normalized NF steering vector, $\mathbf{d}_i = \mathbf{a}(\mathbf{u}_i)/||\mathbf{a}(\mathbf{u}_i)||$, corresponding to a candidate position $\mathbf{u}_i$ on the $g_x \times g_y$ Cartesian grid.

In practice, the computational demand of OMP is significant. Before the correlation stage, the covariance matrix of the received data must be estimated and decomposed to extract $\mathbf{U}_s$, which already involves intensive matrix operations. During the iterative search, the algorithm evaluates the correlation coefficient for every candidate position in the grid, requiring the generation and normalization of thousands of steering vectors and repeated vector–matrix multiplications. This exhaustive evaluation makes OMP substantially more efficient than a full 2D MUSIC scan, yet still computationally expensive when the search grid is dense or the array dimension is large. In the specific case considered here, where a single source is assumed ($K = 1$), the algorithm further simplifies to a single matching stage.

The procedure, as implemented in this study, iterates through each candidate position $\mathbf{p}_i$ on the grid and generates the corresponding dictionary column $\mathbf{d}_i$ on-the-fly using the NF steering vector model from Equation (3). The algorithm then finds the column that is most highly correlated with the signal subspace by maximizing the magnitude of the inner product:

$$\hat{i} = \arg\max_i |\mathbf{d}_i^H \mathbf{U}_s|. \tag{31}$$

The estimated position, $\hat{\mathbf{u}}_k$, is the grid position $\mathbf{u}_{\hat{i}}$ associated with the best-matching column. To ensure the comparison is based on vector shape rather than magnitude, both the signal subspace $\mathbf{U}_s$ and each dictionary column $\mathbf{d}_i$ are normalized to unit norm before the correlation is computed. This entire process is summarized in Algorithm 5. The asymptotic complexity of OMP-NF is discussed in detail in Section 4.11.

Algorithm 5 OMP NF

Input: $\mathbf{Y}$; array geometry; grid parameters-$\mathbf{D}_{\text{NF}}^{\text{norm}}$; λ; K
$L \leftarrow$ number of columns in $\mathbf{Y}$
Compute the mean covariance matrix $\mathbf{R}$
  $\mathbf{R} \leftarrow \frac{1}{L}\mathbf{Y}\mathbf{Y}^H$
Perform eigenvalue decomposition of $\mathbf{R}$
  $(\mathbf{U}, \Lambda) \leftarrow \text{eig}(\mathbf{R})$
Construct the signal subspace $\mathbf{U}_s$
$\mathbf{u}_s^{norm} \leftarrow \mathbf{U}_s / ||\mathbf{U}_s||_2$ {Normalize the input signal subspace for correlation}
1. Initialize search variables
max_corr $\leftarrow -1$ and $\hat{\mathbf{u}}_k \leftarrow$ [NaN, NaN]
2. Iterate through all candidate positions on the grid
for each $\mathbf{u}_i$ in the grid **do**
  Compute steering vector candidate $\mathbf{a}(\mathbf{u}_i)$;
  2.1. Normalize the column;
  $\mathbf{d}_i \leftarrow \mathbf{a}(\mathbf{u}_i) / ||\mathbf{a}(\mathbf{u}_i)||_2$
  2.2. Compute the correlation with the signal subspace
  corr $\leftarrow |\mathbf{d}_i^H \mathbf{u}_s^{norm}|$
  2.3. Update the best candidate if a better match is found
  if corr $>$ max_corr **then**
    max_corr $\leftarrow$ corr
    $\hat{\mathbf{u}}_k \leftarrow \mathbf{u}_i$
  end if
end for
Output: $\hat{\mathbf{u}}_k = [\hat{x}, \hat{y}]$.

4.10. 2D ESPRIT

The 2D ESPRIT algorithm is a search-free subspace method that estimates the source's direction of arrival. It operates under a far-field assumption, modeling the incoming signal as a planar wavefront, and exploits the rotational invariance property of the antenna array. The URA is conceptually divided into two pairs of overlapping SAs, one pair displaced along the x-axis and the other along the z-axis.

Before the formation of these selection matrices, it is necessary for the algorithm to compute the sample covariance matrix $\mathbf{R} \leftarrow \frac{1}{L}\mathbf{Y}\mathbf{Y}^H$ and its eigenvalue decomposition to extract the signal subspace $\mathbf{U}_s$.

These operations dominate the computational load, covariance estimation and the EVD, even though the subsequent stages are search-free [29] .

The algorithm begins by constructing selection matrices that extract the signal subspace components corresponding to each of these four SAs from the full signal subspace, $\mathbf{U}_s$. Using these selected subspaces, two rotational operators, Φ_x and Φ_z, are computed by solving a least-squares problem. The eigenvalues of these operators are directly related to the signal's spatial frequencies.

Finally, a geometric transformation converts the estimated cosines into the source's Cartesian coordinates (x,y) on the ground plane, given the known height of the array. Therefore, although 2D ESPRIT avoids an explicit two-dimensional grid search, the cumulative cost of the covariance estimation, EVD, and pseudoinverse steps keeps its overall computational complexity at a high level. A formal analysis of the computational complexity for 2D ESPRIT is provided in Section 4.11.

4.11. Asymptotic complexity analysis

The following asymptotic complexity (Big-O) analysis is derived by decomposing each algorithm into its fundamental computational operations. The costs are dominated by three main blocks: covariance matrix formation, EVD, and grid search.

The complexity varies across the analyzed localization strategies. In the case of the MUSIC NF method, the entire URA comprising M antenna elements is employed. Consequently, the associated covariance matrix has dimensions M^2, leading to a complexity cost of $O(LM^2)$. Moreover, the spectral decomposition of this matrix introduces an additional complexity of $O(M^3)$. Finally, computing the pseudospectrum on a two-dimensional search grid with G points requires $O(GM^2)$ operations, 2D MUSIC follows the same structure, so it has similar complexity. The overall computational complexity [23,30] can be expressed in Big-O notation, summarizing as follows:

$$O(M^3 + LM^2 + G_f M^2). \tag{32}$$

The adaptive MUSIC strategy reduces complexity by performing an initial coarse estimate that limits the subsequent search region. The complexity, adapted from the complexity of MUSIC NF in Equation 32 including the additional fine search window, is expressed as:

$$O(M^3 + LM^2 + G_c M^2 + G_w M^2). \tag{33}$$

For the PEACH-MUSIC approach, only a single row and column—corresponding to two SA of size $\sqrt{M}$ are processed. Accordingly, the covariance estimation and the eigendecomposition are performed on $\sqrt{M} \times \sqrt{M}$ matrices, incurring computational costs of $O(LM)$ and $O(M^{\frac{3}{2}})$, respectively. The pseudospectrum is then evaluated over G_{peach} positions. Hence, the overall complexity is [10]:

$$O(M^{\frac{3}{2}} + LM + G_{\text{peach}} M). \tag{34}$$

Unlike subspace methods, the DFT NF Beamforming does not require EVD. Its complexity is instead dictated by the brute-force evaluation of the power spectrum Equation (29) over all grid points. This process involves projecting L snapshots of the $M \times 1$ received signal onto each candidate steering vector, leading directly to the computational cost [27]:

$$O(G_f\, LM). \tag{35}$$

The bicubic interpolation strategy stands out by enhancing localization accuracy through post-processing rather than re-evaluating the full pseudospectrum. While it refines the coarse grid to a denser representation, the associated complexity scales linearly with the number of interpolation points and does not involve additional matrix operations [26]:

$$O(M^3 + LM^2 + G_c M^2 + G_w). \tag{36}$$

The cost of 2D ESPRIT is dominated by the linear-algebra operations required for covariance formation, singular-value decomposition, and the pseudoinverse computation of the rotational operators, followed by a final eigenvalue decomposition. Although the method avoids an explicit 2D search, these matrix factorizations maintain a high numerical load. Therefore, the overall computational complexity can be more accurately represented as [29,31]:

$$O(M^3 + LM^2). \tag{37}$$

The complexity of the OMP NF method, as implemented, is dictated by the exhaustive grid evaluation. For each of the G_f candidate positions, he algorithm generates and normalizes a steering vector and computes its inner-product correlation with the signal subspace $\mathbf{U}_s$. Before this loop, covariance estimation and eigendecomposition are also required to obtain $\mathbf{U}_s$, introducing a fixed preprocessing cost. Consequently, the total computational complexity is expressed as [28]:

$$O(G_f M + LM^2 + M^3), \tag{38}$$

where, for all Big-O equations:

- M is the total number of array elements.
- L is the number of temporal snapshots.
- G_f is the number of fine grid points.
- G_c is the number of coarse grid points.
- G_{peach} is the number of grid points to evalueting PEACH.
- G_w: Linear resolution of the refined grid used in bicubic interpolation and adaptive.

The complexities summarized in Table 2 reveal the fundamental trade-offs between the evaluated algorithms. Search-free and decomposition-based techniques (e.g., 2D ESPRIT) exhibit no dependency on grid density but remain constrained by cubic-order matrix operations. Conversely, search-based methods such as OMP and MUSIC scale linearly or quadratically with G, depending on whether they correlate directly with the subspace or evaluate a full pseudospectrum. These contrasting computational behaviors explain the runtime trends reported in the numerical results section.

At the lowest end of the complexity spectrum is the PEACH-MUSIC method. By geometrically decomposing the URA into two orthogonal 1D subarrays (SAs). It circumvents the prohibitive 2D grid search by performing two independent 1D searches, one estimating a circular region and the other a hyperbolic region. The final position is computed analytically from the intersection of these two geometric shapes.

Table 2. Computational complexity of the evaluated localization techniques.

Method	Complexity (Big-O)
2D ESPRIT [29]	$O(M^3 + LM^2)$
OMP NF [28]	$O(M^3 + LM^2 + G_f M)$
PEACH-MUSIC [10]	$O(M^{\frac{3}{2}} + LM + G_{\text{peach}} M)$
DFT NF Beamforming [27]	$O(G_f ML)$
Adaptive MUSIC [23][1]	$O(M^3 + LM^2 + G_c M^2 + G_w M^2)$
Bicubic MUSIC [26]	$O(M^3 + LM^2 + G_c M^2 + G_w)$
MUSIC NF [23]	$O(M^3 + LM^2 + G_f M^2)$
2D MUSIC [23][2]	$O(M^3 + LM^2 + G_f^{\text{FF}} M^2)$

[1]Complexity is a direct adaptation, with search reduction.

[2]FF search grid with the same amount of search points.

The search-based methods have complexities that are primarily dictated by the grid search term G. A critical distinction appears in the complexity of DFT NF Beamforming $O(G_f ML)$, which, unlike the others, includes a dependency on the number of snapshots, L, within its search loop. This factor explains its surprisingly high execution time in our simulations and its linear increase in runtime as L grows, a behavior not present in the other search-based methods whose search costs are independent of L.

The refinement strategies highlight a clear divergence in approach. Adaptive MUSIC pays a significant computational price by performing a second, high-density MUSIC search, making it the most expensive method overall. In stark contrast, Bicubic MUSIC achieves a similar high-resolution result by replacing the costly second search with a computationally negligible interpolation step in reduced window. This explains its excellent balance of accuracy and efficiency. Finally, PEACH-MUSIC demonstrates a unique approach to complexity reduction by applying expensive operations like SVD to much smaller SAs, effectively lowering the polynomial degree of the dominant term from M^3 to $M^{\frac{3}{2}}$.

5. Numerical results

In this section, we present a comprehensive numerical evaluation of the discussed localization strategies. The performance of each algorithm is assessed through Monte Carlo simulations implemented in MATLAB R2023b. The simulated scenario consists of a single ground-level user source emitting a known pilot signal towards an elevated 8×8 URA, assuming a LOS propagation channel. For each simulation run, the user is placed at a random position within a predefined surveillance area to ensure the robustness of the results. The key parameters for the simulation setup, which are common across all experiments unless otherwise specified, are summarized in Table 1.

In the numerical results, the Root-MUSIC algorithm, evaluated as a possible FF baseline, demonstrated significant performance degradation and was found inoperable within our NF model due to its reliance on a plane-wave assumption incompatible with the spherical wavefront and amplitude variations observed. The performance of the remaining methods was assessed across varying SNR levels and snapshot numbers L, with results detailed in Figures 2–9.

The elevation disparity between antenna arrays and users significantly influences the structure and localization properties of the MUSIC pseudospectrum. Unlike conventional setups, in which arrays and

users are located within the same plane (as illustrated in Figure 2a), elevated arrays generate distinctive pseudo-spectral features that markedly enhance the accuracy and effectiveness of localization. Specifically, elevating the antenna array, as shown in Figure 2b, converts the traditional beam-shaped MUSIC pseudospectrum into a distinctly sharp peak. This transformation considerably boosts the precision of localization, facilitating accurate determination of user positions beyond mere Direction-of-Arrival (DoA) estimation. However, this enhanced precision also introduces challenges, as efficiently identifying the pseudospectrum peak becomes more computationally demanding because of the requirement for dense 2D grid evaluations. The overall effect is clearly demonstrated in Figure 2.

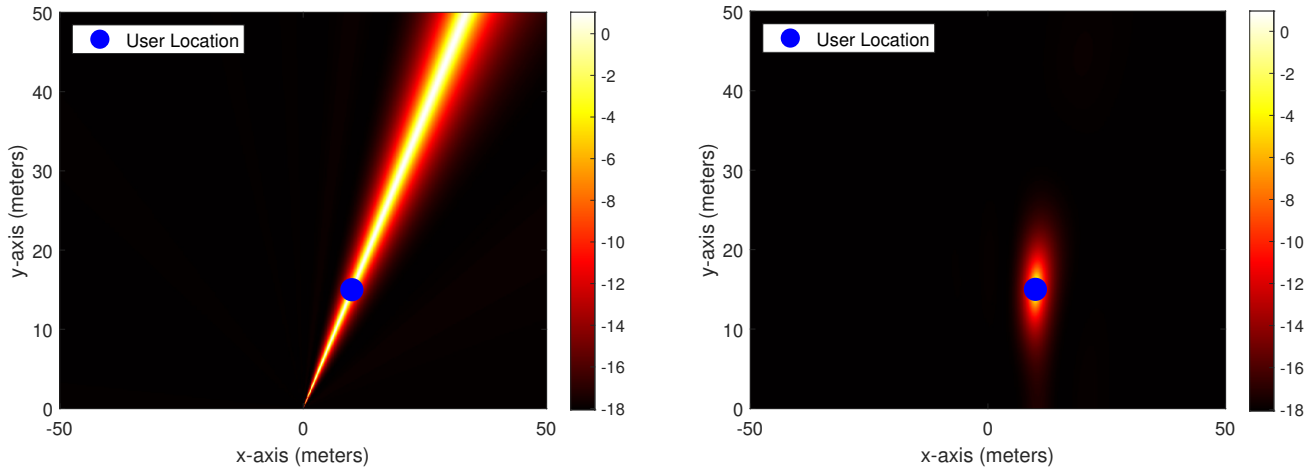

(a) (b)

Figure 2. Comparison of the MUSIC pseudospectrum for different array elevations. An 8×8 element array is used with an SNR of 10 dB and a single user located at $(10, 15, 0)$ m. **(a)** Pseudospectrum of co-planar array at z = 0 m; **(b)** Pseudospectrum of elevated array at z = 20 m. Results show that properly elevating the array increases the accuracy of the location.

The second preliminary analysis addresses the critical trade-off between search grid resolution, estimation accuracy, and computational cost. To achieve high localization accuracy, a dense search grid is necessary, but this comes at a significant computational price.

Figure 3 illustrates this dilemma with MUSIC NF. Figure 3a shows that at sufficient SNR levels ($\geq$ 10 dB), refining the grid side from coarse to fine substantially improves the RMSE. However, Figure 3b reveals the consequence: the average execution time increases exponentially, growing by nearly two orders of magnitude across the tested range. To better quantify the accuracy component of this trade-off, Figure 4 provides a focused comparison of coarse (200×200) and fine (600×600) grids against the theoretical CRB. The finer grid consistently yields a lower RMSE, particularly at higher SNRs, demonstrating its superior accuracy. Nonetheless, this improvement in precision is incremental compared to the exponential increase in runtime shown previously. This analysis confirms that relying on brute-force grid refinement for high precision is computationally prohibitive for many real-time applications. It therefore establishes the motivation for investigating the advanced, low-complexity strategies that are the focus of this paper, which aim to approach the accuracy of a fine grid without incurring its prohibitive execution time.

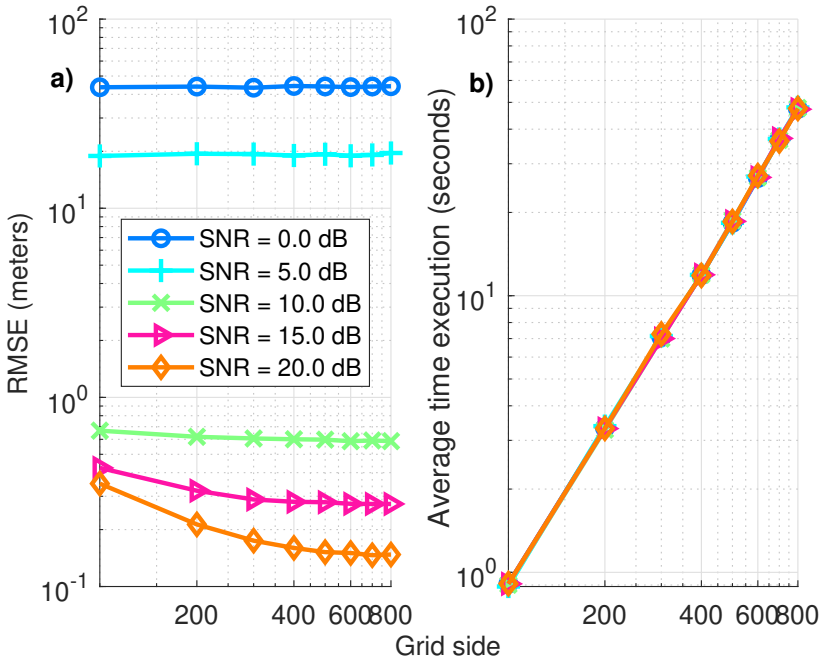

Figure 3. Impact of search grid resolution on MUSIC NF localization performance and computational cost. **(a)** RMSE as a function of the grid side for different SNR levels; **(b)** Average execution time as a function of the grid side. The results highlight the trade-off, showing that increased accuracy from finer grids comes at a significant computational expense.

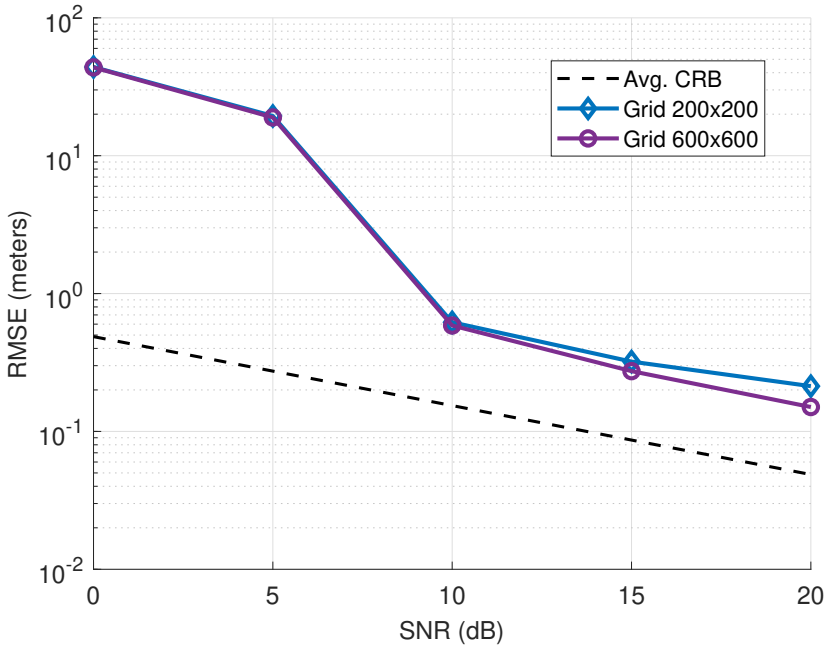

Figure 4. RMSE versus SNR for coarse and fine search grids. The performance of a 200×200 grid is compared against a 600×600 grid, with the average CRB shown as a theoretical benchmark. Results are based on L = 100 snapshots and averaged over 1000 Monte Carlo trials.

The central comparative analysis of this study is presented in Figure 5, which plots the localization RMSE as a function of SNR for all evaluated strategies against the theoretical CRB. As expected, all

methods based on the correct NF model show improved accuracy as the SNR increases. Conversely, the strategies employing a mismatched FF model (2D MUSIC and 2D ESPRIT) exhibit a high error floor > 20 m, confirming their unsuitability for direct localization in the NF and validating the physical modeling choices of this work. The PEACH-MUSIC also presents a significant error, caused by its selection of linear SA that reduces the total number of antennas to M. The high-resolution techniques MUSIC NF, Adaptive Grid, Bicubic Interpolation, DFT NF, and OMP NF regularly demonstrate superior performance, closely aligning with one another, while maintaining a reasonably stable margin from the CRB as the SNR increases. Concentrating on the DFT-NF method, which produces good results at low SNR. The OMP NF methodology, for example, obtained an RMSE of 2.90 m at 15 dB, but the other techniques improved this by $\approx 4\%$ to 2.79 m.

Notably, these high-resolution techniques methods maintain a relatively constant gap to the CRB as the SNR improves. This may suggest the presence of a systematic bias in the estimation, which is not reduced by higher signal power, presenting a potential area for future investigation and calibration. In contrast, PEACH-MUSIC shows significant performance degradation at low and medium SNRs. This increased sensitivity to noise is due to its reliance on 1D SAs (a single row and column), which leverage only $\sqrt{M}$ elements for each parameter estimation, making it less robust than methods using the full 2D array aperture.

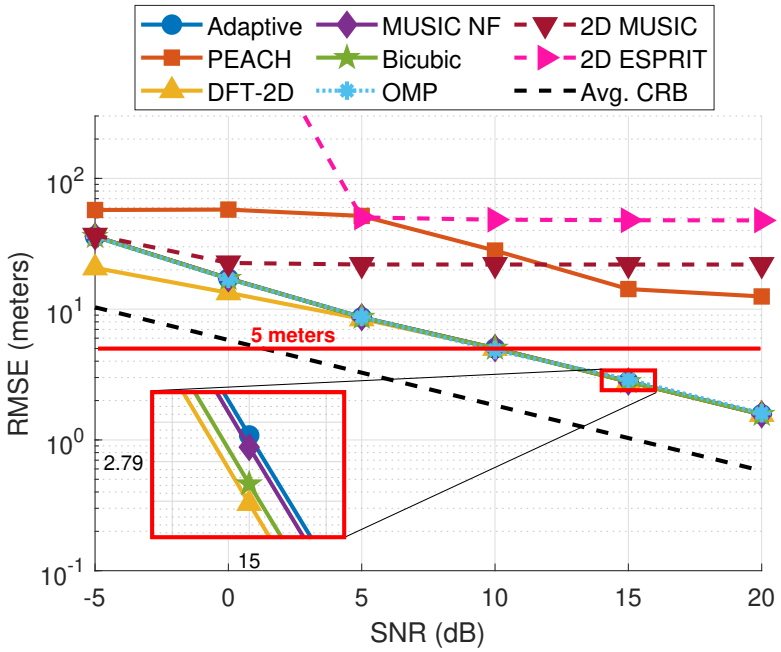

Figure 5. RMSE performance versus SNR for all evaluated localization strategies. The simulation uses an 8 × 8 URA elevated at 20 m with L = 100 snapshots, averaged over 1000 trials. The CRB is shown as a theoretical benchmark. The results highlight the error floor of mismatched far-field models (2D MUSIC/2D ESPRIT) and the convergence of high-resolution techniques at high SNR, which is magnified in the inset.

While accuracy is a primary metric, a complete evaluation must consider computational complexity to understand the practical viability of each method. Figures 6 and 7 provides this complementary analysis. The Figure 6a shows the mean execution time for each algorithm as a function of SNR. The flat curves

confirm that, for all methods, the computational complexity is independent of the noise level. A clear hierarchy in execution speed is evident: the search-free method PEACH-MUSIC and 2D ESPRIT, exhibit mean execution times in the order of milliseconds under the simulated configuration. However, this computational advantage is only viable for PEACH-MUSIC, as 2D ESPRIT does not operate adequately in this scenario due to its reliance on a mismatched far-field model. In contrast, the MUSIC NF method is by far the most computationally intensive, requiring an order of magnitude more time than the other search-based techniques. The Figure 6b plots the calculated log-asymptotic complexity $\log(\text{Big-}O)$ for each algorithm, corroborating the empirical temporal measures presented in Figure 6a, and showing that the complexity is not dependent on the SNR.

The Figure 7 directly visualizes the critical trade-off between accuracy (RMSE) and mean execution time, where the ideal performance is located in the bottom-left corner. This plot is essential for selecting an algorithm based on application constraints. It shows that while PEACH-MUSIC and 2D ESPRIT achieve the lowest execution times among all tested algorithms, for different reasons they do not achieve good estimation accuracy. We consider the RMSE of 5 m, around 10% of the greatest distance of the antenna array, to be good estimation accuracy, marked with the red line. The most effective trade-off is offered by the methods occupying the middle ground. Specifically, bicubic interpolation and provide a compelling balance, in high SNR achieving under 5 meters accuracy comparable to the most complex methods but with a mean execution time of almost 1 second.

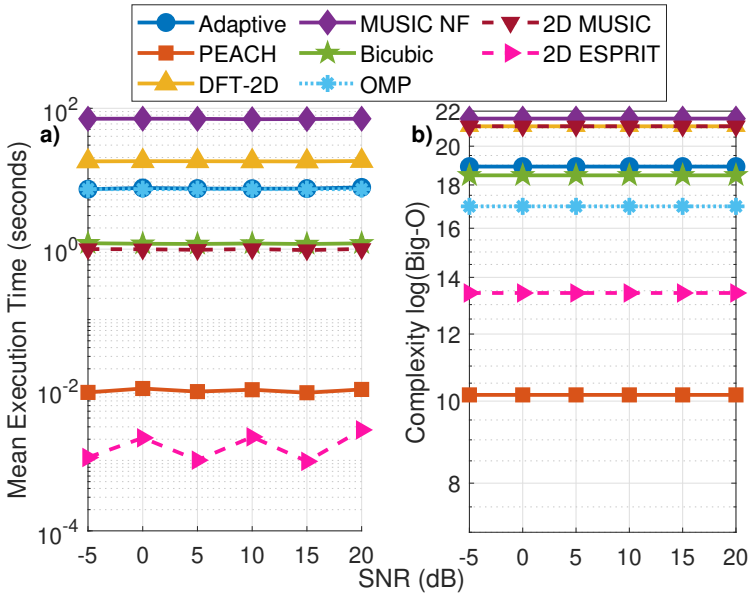

Figure 6. Computational complexity and performance trade-off analysis. **(a)** Mean execution time versus SNR for each algorithm, demonstrating that complexity is largely independent of noise levels; **(b)** Calculated log-asymptotic complexity $\log(\text{Big-}O)$ for each algorithm, corroborating the empirical temporal measures across the tested SNR range $[-5, 20]$ dB.

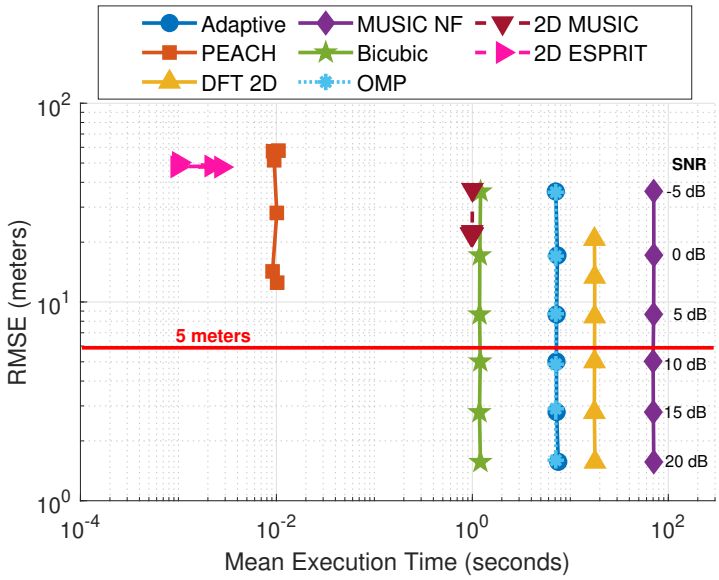

Figure 7. Trade-off between accuracy (RMSE) and time (mean execution). M = 8 × 8 URA elevated at 20 m with L = 100 snapshots. Each point cloud represents the performance of an algorithm across the tested SNR range [−5, 20] dB.

In addition to SNR, the number of available snapshots (L) directly impacts the reliability of the covariance matrix estimation and, consequently, the localization accuracy. Figure 8 illustrates the RMSE performance as a function of L for all evaluated methods, simulated at a fixed SNR of 15 dB. As shown, the accuracy of all high-resolution near-field methods; MUSIC NF, Adaptive, Bicubic, OMP NF, and DFT-NF improves significantly as L increases. A larger dataset provides a more robust estimate of the signal and noise subspaces, leading to a reduction in RMSE from approximately 4–5 meters at L = 50 to just over 1.3 meters at L = 500.

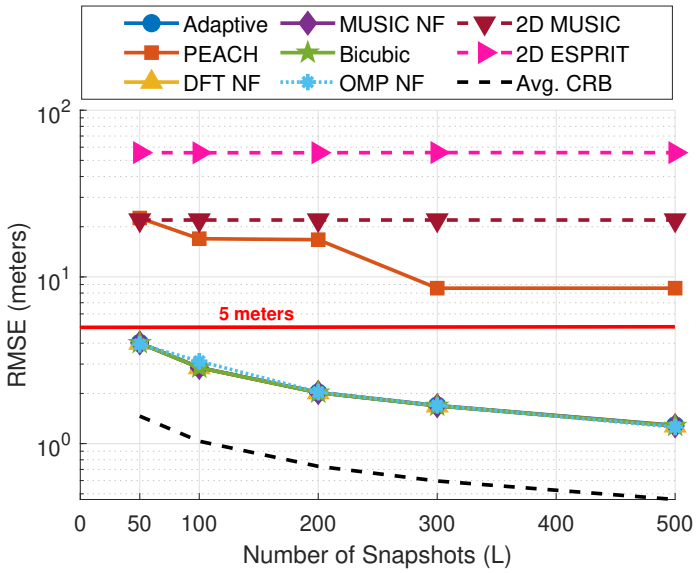

Figure 8. RMSE performance versus the number of snapshots (L). The simulation was conducted at a fixed SNR of 15 dB, using an 8 × 8 URA elevated at 20 m. The results show that a larger number of snapshots improves accuracy for all valid NF methods by enabling a more robust covariance matrix estimation. The performance of mismatched models remains poor, indicating that more data cannot compensate for an incorrect physical model.

On the other hand, the performance of the mismatched FF models; 2D MUSIC and 2D ESPRIT shows little to no significant improvement, remaining poor across the entire range of L PEACH-MUSIC has an interesting improvement as L grows, but it is affected by the low number of $2 \times \sqrt{M}$ antennas it uses. This demonstrates that for these methods, the primary limitation is either an incorrect physical model or high sensitivity to noise, weaknesses that cannot be overcome simply by increasing the number of snapshots. This analysis confirms that both sufficient SNR and an adequate number of snapshots are crucial to achieving high-precision localization but penalized in complexity.

The impact of the number of snapshots on computational cost is detailed in Figure 9. As shown in panel Figure 9a, the execution time for most of the evaluated methods remains remarkably stable and largely independent of the number of snapshots. This indicates that for these algorithms, the dominant computational cost lies in operations that do not scale with L, such as the eigenvalue decomposition or the grid search. The notable exception is the DFT NF method, which shows a clear increase in runtime as L grows. Figure 9b illustrates the computed log-asymptotic complexity log(Big-O) for each method, validating the empirical temporal metrics displayed in Figure 9a and indicating that complexity in most cases is little affected by L, with the exception of DFT.

The trade-off, illustrated in Figure 10, is therefore highly favorable. The significant improvement in accuracy gained from using more snapshots (the vertical drop in RMSE) comes at a negligible cost in execution time for most methods. This confirms that, when possible, acquiring a larger number of snapshots is a highly efficient strategy for improving localization performance.

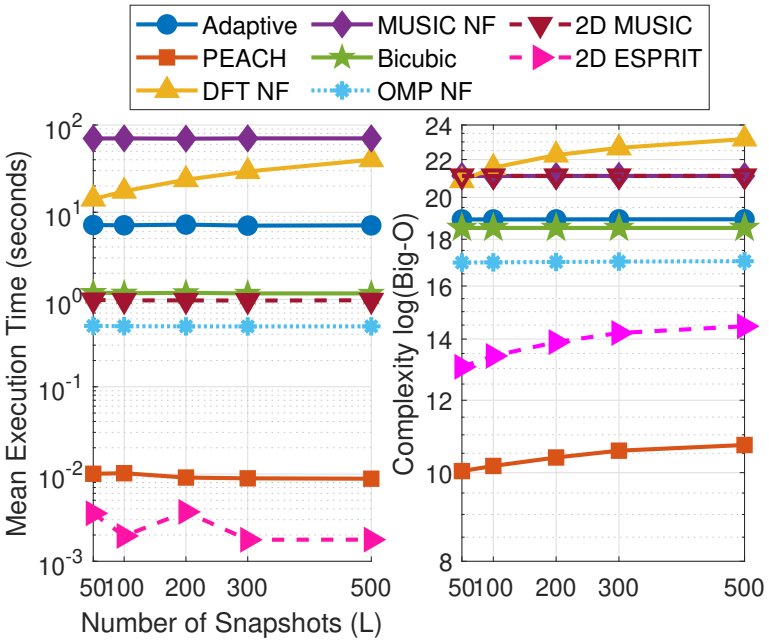

Figure 9. Impact of the number of snapshots (L) on computational complexity and performance trade-off. The simulation was conducted at a fixed SNR of 15 dB. **(a)** Mean execution time versus L, showing a modest increase in runtime for larger datasets in DFT NF; **(b)** Calculated log-asymptotic complexity log(Big-O) for each algorithm, corroborating the empirical temporal measures across the tested L range [50 100 200 300 500].

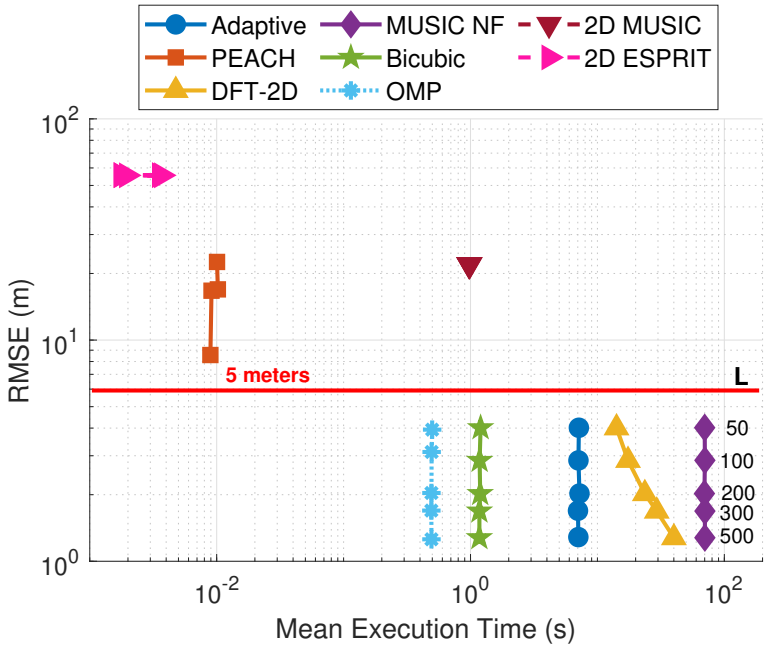

Figure 10. Trade-off between accuracy (RMSE) and time (mean execution). M = 8×8 URA elevated at 20 m with SNR = 15 dB. Each point represents the performance of an algorithm across the tested L range [50 100 200 300 500].

6. Conclusion

This study quantitatively mapped the accuracy–complexity landscape of 2D localization under an elevated URA using a NF (spherical-wave) formulation that is physically consistent with direct position estimation. Elevating the array sharpens the MUSIC pseudospectrum peak and improves localizability, but it also makes peak search more compute-intensive due to the need for denser 2D evaluations. This trade-off was explicitly evidenced by the grid-resolution experiments Figure 4, where finer grids reduce RMSE yet drive orders-of-magnitude increases in runtime.

Across algorithms, three robust patterns emerge. First, near-field consistent methods (MUSIC NF, Adaptive refinement, Bicubic-assisted MUSIC, OMP NF, and DFT-NF) display the expected RMSE decrease with SNR. Conversely, far-field baselines (2D MUSIC and 2D ESPRIT) exhibit a clear error floor from model mismatch in this localization setting Figure 5, validating the necessity of the NF formulation. Second, snapshot-rich regimes (larger L) substantially tighten RMSE for the valid NF methods–down to ≈ 1.3 m at $L = 500$ in the reported setup–while the mismatched baselines and PEACH show limited gains Figure 8. Third, runtime is largely SNR-invariant for most methods; complexity is governed by grid size, subspace operations, and search strategy Figures 6 and 9.

OMP NF reached accuracy close to the refined MUSIC family (e.g., RMSE ≈ 2.90 m at 15 dB, *vs.* ≈ 2.79 m for other high-resolution methods) at a significantly lower runtime, positioning it as a pragmatic "middle-ground" option. Adaptive (zoom-in) MUSIC achieves high precision by restricting fine search to a window, but it is the most compute-hungry among the refinements.

Within this landscape, the Bicubic-assisted MUSIC refinement consistently converts a coarse pseudospectrum ($200 \times 200 = 40$ k points) into estimates approaches fine-grid accuracy ($600 \times 600 = 360$ k points) with negligible additional cost. In the reported experiments, it delivered

$\approx 4\%$ RMSE reduction at 15 dB relative to the coarse grid in MUSIC NF, while avoiding the $\sim$8 times burden of a full fine-grid recomputation. OMP NF reached accuracy close to the refined MUSIC family (e.g., RMSE ≈ 2.90 m at 15 dB, *vs.* ≈ 2.79 m for other high-resolution methods) at a significantly lower runtime, positioning it as a pragmatic "middle-ground" option. Adaptive (zoom-in) MUSIC achieves high precision by restricting fine search to a window, but it is the most compute-hungry among the refinements. However, its use of only $\sqrt{M}$-element apertures per dimension makes it less robust, exhibiting significant performance degradation at low-moderate SNR.

From a complexity perspective, the asymptotic complexity (Table 2) match the empirical timing Figures 6b and 9b. PEACH-MUSIC, based on orthogonal 1D SAs and geometric intersection, attains the lowest asymptotic burden and the fastest measured execution. However, its use of only $\sqrt{M}$-element apertures per dimension makes it less robust, exhibiting significant performance degradation at low-moderate SNR.

It is crucial to contextualize these findings within the study's modeling assumptions: a single signal source ($K = 1$) and an ideal free-space LOS propagation channel. For the target ISAC paradigm, these trade-offs dictate operational viability. While PEACH-MUSIC offers the lowest latency, its poor robustness may be unacceptable for mission-critical sensing. Conversely, the Bicubic-assisted MUSIC and OMP NF methods provide a compelling balance of accuracy and efficiency, though their execution times (on the order of one second in this setup) may still challenge real-time applications requiring high update rates. Furthermore, a critical anomaly was observed: all high-resolution NF methods maintained a persistent RMSE gap to the CRB, even at high SNR. This suggests a potential systematic estimation bias—unmitigated by signal power—whose origin is undetermined.

Future work must therefore prioritize extending this analysis beyond these idealized boundaries. This includes evaluating the robustness and scalability of the most promising algorithms (e.g., Bicubic-MUSIC, OMP NF) in more complex operational scenarios, specifically multi-source (multi-user) environments and non-line-of-sight (NLOS) propagation conditions. Furthermore, it is necessary to rigorously investigate the source of the systematic estimation bias. Determining whether this bias is inherent to the NF steering vector model, an artifact of the subspace decomposition in this elevated URA geometry, or a consequence of the grid-based search itself is essential for developing localization strategies that can truly approach the theoretical CRB.

Acknowledgments

This work was supported by the CAPES in Program 13179-PDPG-Strategic Postdoctoral Program by process 88887.983958/2024-00.

Authors' contribution

Thiago Augusto Bruza Alves: conceptualization, data curation, formal analysis, investigation, methodology, software, validation, visualization, writing—original draft and writing—review & editing. Bruno Felipe Costa: formal analysis, investigation, methodology, software and writing—original draft. Taufik Abrão: funding acquisition, project administration, resources, supervision, writing—original draft and writing—review & editing. All authors have read and agreed to the published version of the manuscript.

Conflicts of interests

Prof. Taufik Abrao holds the position of Associate Editor for *Electronics and Signal Processing* and has not peer reviewed or made any editorial decisions for this paper.

Nomenclature

Nomenclature	Description
CRB	Cramér–Rao bound
DFT	Discrete fourier transform
DoA	Direction of arrival
ESPRIT	Estimation of signal parameters via rotational invariance techniques
EVD	Eigenvalue decomposition
FF	Far field
FIM	Fisher information matrix
ISAC	Integrated sensing and communication
LOS	Line of sight
MIMO	Multiple-input and multiple-output
MUSIC	Multiple signal classification
NF	Near field
NLOS	Non line-of-sight
OMP	Orthogonal matching pursuit
PDF	Probability density function
PEACH	Position estimation using circle and hyperbola
RMSE	Root mean square error
SA	Subarray
SNR	Signal-to-noise ratio
SVD	Singular value decomposition
ULA	Uniform linear array
UPA	Uniform planar array
URA	Uniform rectangular array
TTD	Tensor train decomposition
XR	Extended reality

List of symbols

Symbol	Description
$\mathbf{a}(\mathbf{u}_k)$	Steering vector for the user position $\mathbf{u}_k$.
$\mathbf{a}_{\text{FF}}(\theta,\phi)$	Far-field (FF) steering vector.
α	Sparse coefficient vector in the OMP formulation.
c	Absolute x-coordinate of the symmetric endpoints of the horizontal SA.
$CRB(x), CRB(y)$	Cramér-Rao Bound for the x and y coordinates.
$\mathbf{d}_i$	i-th column of a dictionary, representing a steering vector.
d_m	Euclidean distance between the user k and the m-th antenna element.
d_{xy}	Radius of the circular region estimated by the vertical SA in PEACH-MUSIC.
Δ	Distance difference characterizing the hyperbolic region in PEACH-MUSIC.
δ_m	Diff. in the x-coord. between the user and the m-th antenna element ($x - x_m$).
$\mathbf{D}$	Dictionary matrix containing steering vectors for candidate positions.
$\mathbf{D}_{\text{FF}}$	Dictionary generated under the far-field (FF) assumption.
$\mathbf{D}_{\text{NF}}$	Dictionary generated under the near-field (NF) assumption.
$\mathbf{D}_{\text{NF}}^{\text{norm}}$	Normalized near-field dictionary.
$\mathbb{E}[\cdot]$	Expectation operator.
ε	Noise tolerance parameter in the OMP optimization problem.
f_c	Operating carrier frequency.
ϕ	Azimuth angle.
Φ_x, Φ_z	Rotational operators in the 2D ESPRIT algorithm.
G	Total number of candidate positions (grid points) in the search grid.
G_c	Number of points in the coarse search grid.
G_f	Number of points in the fine search grid.
G_{peach}	Number of grid points for the PEACH evaluation.
G_w	Number of grid points within the refinement window (Adaptive MUSIC).
g_x, g_y	Number of grid points along the x and y axes, respectively.
$\mathbf{J}(\mathbf{u}_k)$	Fisher Information Matrix (FIM).
J_{xx}, J_{yy}, J_{xy}	Components of the Fisher Information Matrix.
K	Number of signal sources (assumed to be 1).
L	Number of temporal snapshots.
λ	Carrier wavelength.
Λ	Diagonal matrix containing the eigenvalues of the covariance matrix.
M	Total number of antenna elements in the array.
N	$M \times L$ matrix of additive white Gaussian noise (AWGN).
N_c	Side dimension of a square search grid ($G_c = N_c^2$).
$\mathbf{n}(t)$	Additive white Gaussian noise (AWGN) vector.
$p(\cdot)$	Probability Density Function (PDF).

Symbol	Description
$\mathbf{p}_m$	Position vector of the m-th antenna element.
$P(x_i, y_i)$	MUSIC pseudospectrum value at position (x_i, y_i).
$P_{DFT}(u_i)$	DFT beamformer power output for the candidate position u_i.
P_{norm}	Normalization constant used in the FIM calculation.
ψ_0	Differential phase offset.
$\mathbf{R}$	Covariance matrix of the received signal.
$\mathbf{R}_h, \mathbf{R}_v$	Covariance matrices for the horizontal and vertical SAs (PEACH).
r_i	Range to the i-th candidate position on the grid.
s	Magnitude of the transmitted pilot signal.
$s(t)$	Known pilot signal transmitted by the user.
σ_n^2	Noise variance.
θ	Elevation angle.
$\text{Tr}(\cdot)$	Trace operator of a matrix.
$\mathbf{u}_k$	Position vector of the k-th user.
$\hat{\mathbf{u}}_k$	Estimated user position.
$\mathbf{U}$	Matrix containing the eigenvectors of the covariance matrix.
$\mathbf{U}_h, \mathbf{U}_v$	Noise subspaces for the horizontal and vertical SAs (PEACH).
$\mathbf{U}_n$	Noise subspace.
$\mathbf{U}_s$	Signal subspace.
W_x, W_y	Size of the refined search window along the x and y axes.
(x_c, y_c)	Coarse position estimate.
$\mathbf{Y}$	$M \times L$ matrix containing all snapshots of the received signal.
$\mathbf{y}(t)$	Received signal vector at time instant t.
$\mathbf{Y}_h, \mathbf{Y}_v$	Data from the horizontal and vertical SAs (PEACH).
$\tilde{z}_m$	Average height of the antenna configuration.
$\|\|\cdot\|\|_0$	ℓ_0-norm, which counts the number of non-zero elements of a vector.
$(\cdot)^H$	Conjugate transpose (Hermitian) operator.
$(\cdot)^{\text{T}}$	Transpose operator.

References

[1] Xiao Z, Zeng Y. An overview on integrated localization and communication towards 6G. *Sci. China Inf. Sci.* 2021, 65(3):131301.

[2] Liang J, Liu D. Joint elevation and Azimuth direction finding using L-shaped array. *IEEE Trans. Antennas Propag.* 2010, 58(6):2136–2141.

[3] Schmidt R. Multiple emitter location and signal parameter estimation. *IEEE Trans. Antennas Propag.* 1986, 34(3):276–280.

[4] Gentilho E, Scalassara PR, Abrão T. Direction-of-arrival estimation methods: a performance-complexity

tradeoff perspective. *J. Signal Process. Syst.* 2020, 92(2):239–256.

[5] Wu S, Luo J, Liu Y. A method for recognition of spectrum peaks in 2-D MUSIC algorithm. In *2005 IEEE International Symposium on Microwave, Antenna, Propagation and EMC Technologies for Wireless Communications*, Beijing, China, August 8–12, 2005, pp. 704–707.

[6] Liu Y, Wu M, Wu S. Fast OMP algorithm for 2D angle estimation in MIMO radar. *Electron. Lett.* 2010, 46:444–445.

[7] Albagory Y. An approach for efficient two-stage 2D-DOA estimation in high-altitude platforms mobile communications. *Prog. Electromagn. Res. C* 2014, 55:115–127.

[8] Wang A, Liu L, Zhang J. Low complexity direction of arrival (DoA) estimation for 2D massive MIMO systems. In *2012 IEEE Globecom Workshops*, Anaheim, USA, December 3–7, 2012, pp. 703–707.

[9] Zhou Y, Fei Z, Yang S, Kuang J, Chen S, *et al.* Joint angle estimation and signal reconstruction for coherently distributed sources in massive MIMO systems based on 2-D unitary ESPRIT. *IEEE Access* 2017, 5:9632–9646.

[10] Costa BF, Abrão T. A low-complexity geometric PEACH approach for 3D localization under elevated planar arrays. In *2025 IEEE International Mediterranean Conference on Communications and Networking (MeditCom)*, Nice, France, July 7–10, 2025, pp. 1–6.

[11] Zoltowski M, Wong K. ESPRIT-based 2-D direction finding with a sparse uniform array of electromagnetic vector sensors. *IEEE Trans. Signal Process.* 2000, 48(8):2195–2204.

[12] Gast A, Magoarou LL, Shlezinger N. Near field localization via AI-aided subspace methods. *arXiv* 2025, arXiv:2504.00599.

[13] Xie Q, Wang Z, Wen F, He J, Truong TK. Coarray tensor train decomposition for bistatic MIMO radar with uniform planar array. *IEEE Trans. Antennas Propag.* 2025, 73(8):5310–5323.

[14] Han S, Al-Jarrah MA, Alsusa E. Pilot-aided simultaneous communication and localisation (PASCAL) under practical imperfections. *arXiv* 2024, arXiv:2311.18762.

[15] Monemi M, Rasti M, Latva-Aho M. Revisiting the Fraunhofer and Fresnel boundaries for phased array antennas. In *GLOBECOM 2024—2024 IEEE Global Communications Conference*, Cape Town, South Africa, December 8–12, 2024, pp. 4744–4749.

[16] Huang YD, Barkat M. Near-field multiple source localization by passive sensor array. *IEEE Trans. Antennas Propag.* 1991, 39(7):968–975.

[17] Zhang X, Zhang H. Hybrid reconfigurable intelligent surfaces-assisted near-field localization. *IEEE Commun. Lett.* 2023, 27(1):135–139.

[18] Balanis CA. *Antenna Theory: Analysis and Design*, 4th ed. Hoboken: Wiley, 2016.

[19] Ding S, Chen B, Li J, Tan J, Yao J, *et al.* Channel measurements for integrated sensing and communication: method and prototype test. In *2024 IEEE 99th Vehicular Technology Conference (VTC2024-Spring)*, Singapore, June 24–27, 2024, pp. 1–6.

[20] Chai Z, Zhang Y, Liu G, Liu Y, Wang J, *et al.* Empirical path loss channel modeling at 28 GHz for integrated sensing and communication system. In *2023 International Conference on Wireless Communications and Signal Processing (WCSP)*, Hangzhou, China, November 2–4, 2023, pp. 366–370.

[21] Yang W, Chen Y, Cardona N, Zhang Y, Yu Z, *et al.* Integrated sensing and communication channel modeling and measurements: requirements and methodologies toward 6G standardization. *IEEE Veh. Technol. Mag.* 2024, 19(2):22–30.

[22] Schmidt R. Multiple emitter location and signal parameter estimation. *IEEE Trans. Antennas Propag.* 1986, 34(3):276–280.

[23] Meng H, Zheng Z, Yang Y, Liu K, Ge Y. A low-complexity 2-D DOA estimation algorithm for massive MIMO systems. In *2016 IEEE/CIC International Conference on Communications in China (ICCC)*, Chengdu, China, July 27–29, 2016, pp. 1–5.

[24] Ramezani P, Demir OT, Björnson E. Localization in Massive MIMO networks: from near-field to far-field. *arXiv* 2024, arXiv:2402.07644.

[25] Swindlehurst A, Kailath T. A performance analysis of subspace-based methods in the presence of model errors. I. The MUSIC algorithm. *IEEE Trans. Signal Process.* 1992, 40(7):1758–1774.

[26] Bruza Alves TA, Abrão T, Marinello JC, Guerra DWM. Complexity-reduced MUSIC using bicubic interpolation to ISAC in near-field region. In *XLIII Simpósio Brasileiro de Telecomunicações e Processamento de Sinais*, Natal, Brazil, September 29–October 2, 2025, pp. 1–5.

[27] Elbir AM, Mishra KV, Vorobyov SA, Heath RW. Twenty-five years of advances in beamforming: from convex and nonconvex optimization to learning techniques. *IEEE Signal Process Mag.* 2023, 40(4):118–131.

[28] Cai TT, Wang L. Orthogonal matching pursuit for sparse signal recovery with noise. *IEEE Trans. Inf. Theory* 2011, 57(7):4680–4688.

[29] Jung Y, Jeon H, Lee S, Jung Y. Scalable ESPRIT processor for direction-of-arrival estimation of frequency modulated continuous wave radar. *Electronics* 2021, 10(6):695.

[30] Golub GH, Loan CFV. *Matrix Computations*, 4th ed. Baltimore: Johns Hopkins University Press, 2013.

[31] Qian C, Huang L, So H. Computationally efficient ESPRIT algorithm for direction-of-arrival estimation based on Nyström method. *Signal Process.* 2014, 94:74–80.